



Analysis of a plasma reactor performance for direct nitrogen fixation by use of three-dimensional simulations and experiments

Downloaded from: <https://research.chalmers.se>, 2025-08-06 16:10 UTC

Citation for the original published paper (version of record):

Tatar, M., Vikash, V., Iqbal, M. et al (2024). Analysis of a plasma reactor performance for direct nitrogen fixation by use of three-dimensional simulations and experiments. Chemical Engineering Journal, 497. <http://dx.doi.org/10.1016/j.cej.2024.154756>

N.B. When citing this work, cite the original published paper.



Analysis of a plasma reactor performance for direct nitrogen fixation by use of three-dimensional simulations and experiments

Massoud Tatar^a, Vikash Vashisth^a, Muzammil Iqbal^b, Thomas Butterworth^b, Gerard van Rooij^b, Ronnie Andersson^{a,*}

^a Department of Chemistry and Chemical Engineering, Chalmers University of Technology, SE-41296, Gothenburg, Sweden

^b Faculty of Science and Engineering, Maastricht University, 6229 GS Maastricht, the Netherlands

ARTICLE INFO

Keywords:

Nitrogen fixation
Plasma reactor
Computational fluid dynamics
Chemical reactions
Residence time distribution

ABSTRACT

This study utilizes state-of-the-art in-situ measurements and advanced three-dimensional simulations to investigate the operation of a microwave plasma reactor for nitrogen fixation at a high subatmospheric pressure under various power inputs. It is shown that the system should be treated as a warm plasma due to negligible differences in vibrational and rotational temperatures and that it is required to account for chemical non-equilibrium. Complex flow field and significant temperature and concentration gradients are observed, emphasizing the need for three-dimensional simulations to accurately describe the interactions between mass, heat, and momentum transport and chemical reactions in non-equilibrium conditions. The innermost plasma regions reach temperatures close to 6000 K, while wall temperatures remain low due to presence of a low-temperature swirling flow field around the hot core. Analysis reveals that the swirling flow field around the hot core provides intrinsic partial quenching in regions with large temperature gradients which counteract the return to chemical equilibrium and enrich the flow surrounding the hot core. The inner flow exhibits a recirculation zone, stagnation point, and a transition into an increasingly parabolic flow profile closer to the reactor outlet. The agreement between the numerical modeling and the measurements is strong. In-situ Raman spectroscopy measurements confirm the calculated temperature field inside the reactor. Thermocouple measurements on the reactor wall are also in good agreement with the simulation. Additionally, Fourier-transform infrared spectroscopy measurements agree very well with the simulated amount of nitrogen oxide exiting the reactor at different microwave power inputs. The understanding and modeling capabilities are expected to support the development of future reactor designs that can facilitate higher yields.

1. Introduction

Extensive research has been devoted to exploring sustainable industrial solutions for nitrogen fixation (NF). These efforts are driven by the pressing need to address the rising demand for agricultural fertilizers, critical for meeting the food requirements of a growing global population. Various approaches have been taken by researchers including the Haber-Bosch (H-B) process, plasma synthesis, biological and metalcomplex NF. An extensive review of each existing process and alternative methods for NF along with the associated challenges has been given by Cherkasov, et al. [1]. Another informative literature review on the energy efficiency and different mechanisms of NO formation including the famous Zeldovich pathway is provided in [2]. In the field of plasma NF, the formation of nitrogen oxide (nitric acid) or ammonia is

achieved as the product of the reaction between nitrogen with oxygen or hydrogen. In this approach, air as the raw material is widely available at a low cost. A detailed historical review of plasma NF is reported in [3,4]. Different types of plasma reactors were adopted by researchers to study nitrogen fixation experimentally. This includes various discharge reactors such as dielectric barrier, glow, spark, and extending arc discharge [5–9] and microwave systems [10–13] to examine NO_x's efficiency and production cost. Saksono, et al. [14] employed the air plasma electrolysis method to inject air into the plasma zone in a K₂SO₄ electrolyte solution to produce NF compounds. Fromentin, et al. [15] studied the effect of adding N₂ on carbon dioxide dissociation and the vibrational kinetics of CO₂ and CO under various non-equilibrium plasma conditions. Majeed, et al. [16] investigated the effect of thermal gas quenching on NF by using a rotating arc plasma. The NO_x yield,

* Corresponding author.

E-mail address: ronnie.andersson@chalmers.se (R. Andersson).

<https://doi.org/10.1016/j.cej.2024.154756>

Received 15 June 2024; Received in revised form 25 July 2024; Accepted 10 August 2024

Available online 15 August 2024

1385-8947/© 2024 The Authors. Published by Elsevier B.V. This is an open access article under the CC BY license (<http://creativecommons.org/licenses/by/4.0/>).

energy cost, and NO_x selectivity were achieved for various operating conditions. Bayer, et al. [17] reported different pathways and timescales relevant to plasma-assisted N_2 and O_2 reactions by measuring the consumption of plasma-derived N and the formation of NO in the gas phase and over Ag catalytic surfaces. Microwave plasma systems have also been extensively utilized for inactivation and destruction of bacteria and viruses. A review of the methods of generating reactive oxygen species through cold atmospheric plasma technique is available in [18]. A study was done on the role of reactive nitrogen species in bacterial killing by developing a microwave plasma system with increased sterilization efficiency [19]. In another work, a microwave plasma system was employed for the generation of a high amount of gaseous nitric oxide to prepare nitric oxide-enriched plasma-activated water to investigate the corresponding effects on coronaviruses [20].

To fully investigate the coupling between the flow, temperature, species, and turbulence fields inside any reactor type with the associated chemistry governing the reactions for plasma production, extensive attention has been paid to the mathematical modeling of such complex systems. This approach provides an understanding of the interactions between the underlying physical and chemical phenomena which are almost impossible to capture experimentally in such rapid dynamic systems with very small time scales [21–24]. A comprehensive review of different numerical strategies for plasma modeling such as electron energy distribution function, Monte-Carlo particle modeling, dynamic modeling, and fluid model is reported by Van Dijk, et al. [23]. A review of numerical modeling of plasma gasification is given by Sedej and Mbonimpa [24] in which the goal is to generate clean energy through a safe destruction of hazardous waste. Wang, et al. [25] reported a comprehensive zero-dimension kinetic model for modeling the plasma-catalytic dry reforming. Wang, et al. [9] proposed a zero-dimension detailed chemical kinetics model for the synthesis of nitrogen oxide at atmospheric pressure and compared the results with a pulsed-power gliding-arc reactor. A numerical study of CO_2 conversion using a microwave plasma model in COMSOL was reported by Ong, et al. [26] at 1 to 3 Torr. Abdollahzadeh, et al. [27] implemented a plasma-fluid model into a compressible flow solver in OpenFOAM for a low-pressure dielectric-barrier discharge and reported the spatial and temporal numerical challenges and the need to have extremely small integration steps. Van Alphen, et al. [7] investigated numerically and experimentally the application of an effusion nozzle for energy-efficient NO_x (NO , NO_2) production in a rotating gliding arc plasma reactor. The computational fluid dynamics (CFD) module in COMSOL was used to solve the bulk gas flow and heat transfer where chemical kinetics was solved with a more advanced version of the zero-dimension model ZDplaskin widely used in literature [28]. A quasi-one-dimensional (1D) method via a streamline-integration technique was adopted to allow the calculation of chemical reactions and the NO_x yields. However, the chemical species are not advected by the 3D flow pattern which is needed for a comprehensive description and analysis of the reactor performance. In another work, several quenching nozzles were numerically studied using quasi-1D chemical kinetics to investigate the effects of rapid gas cooling after the plasma for quenching the CO recombination reactions [29]. A magnetohydrodynamic numerical analysis of argon plasma gas swirl was conducted by Perambadur, et al. [30] to investigate the fluid motion and the contact pattern of the plasma with a secondary gas in OpenFOAM where no chemistry was involved in the simulations.

As inferred from the literature, some studies have applied zero or one-dimensional kinetics modeling due to the complexity and number of chemical reactions used for modeling the plasma reactor. Thus, the realistic distribution of chemical species, temperature, and residence time distribution which has great importance from a reaction engineering point of view should be addressed to provide better insight into the reactor performance. It is worth mentioning that there are some numerical studies dedicated to fully coupling the flow and energy transport equations with the electromagnetic field by incorporating the Maxwell equations. However, the chemistry and the reaction modeling

have been excluded and the working fluid is treated as a single gas component. Moreover, in some other numerical investigations of the plasma systems, the continuity and momentum equations are solved for electrons and ions at Torric pressure levels but not at higher pressure.

In this study, three-dimensional numerical modeling of a microwave plasma reactor is conducted, and the results are compared with the experimental data. A mixture of N_2 and O_2 is imposed at tangential inlets creating a swirling flow to stabilize the core and protect the reactor walls. The governing equations for momentum, energy, and species transport are coupled with five-species chemical kinetics to account for the chemical non-equilibrium reactions aiming at computing the temperature field and nitric oxide mole fraction distributions inside and at the outlet of the reactor. Simulations are performed in ANSYS Fluent, and validation is done with experimental measurements using in-situ Raman spectroscopy and Fourier-transform infrared spectroscopy (FTIR).

2. Experimental methodology

The experimental plasma reactor setup and the in-situ Raman spectroscopy measurements are described in this section.

2.1. Plasma reactor setup

The plasma reactor consists of a 26 mm internal diameter quartz glass tube inserted into a WR340 waveguide, powered by a 2.45 GHz 3 kW solid-state microwave power source. We use dried compressed air at a total flow rate of 20 standard liters per minute (SLM), and reactor pressure is set to 0.65 Bar, with a fixed plasma power of 400 W. The gas is fed tangentially into the reactor tube in the so-called “forward vortex configuration” which is required to stabilize the plasma in the radial tube center. The NO_x concentration is monitored using a Bruker Invenio R FTIR with an MCT detector with the gas cell maintained at ~ 0.2 Bar to minimize line broadening and prevent condensation of N_2O_4 . The plasma rovibrational temperature is monitored using in-situ Raman spectroscopy, described in the next section. Similar reactors with in-situ laser scattering are described also in [31,32]. A diagram of the experimental setup is shown in Fig. 1.

2.2. Raman spectroscopy

We use spontaneous Raman spectroscopy to quantify the vibrational and rotational temperature of N_2 within the plasma. The Raman system uses the 532 nm 2nd harmonic of an injection seeded Nd:YAG laser (Amplitude Powerlite 9030), with a pulse duration of about 8 ns, and pulse energies of about 500 mJ at a 30 Hz repetition frequency. The vertically polarized laser beam is directed along the reactor's axis and softly focused using a pair of perpendicular cylindrical lenses with $f = 1.75$ m to avoid laser-induced breakdowns or non-linear optical effects. The scattered light from the laser is collected perpendicular to the beam on the horizontal plane, where it is collimated using a 25.4 mm diameter, $f = 100$ mm lens. Rayleigh scattering and stray laser light are suppressed by passing the collimated light through an ultra-steep long-pass edge filter (Semrock Razor Edge) with $> \text{OD}6$ above 536.4 nm. The collimated light is focused onto a custom fibre bundle of $19 \times 200 \mu\text{m}$ that leads to a commercial Czerny-Turner spectrometer (Andor Kymera 328i), equipped with an ICCD camera. For these measurements, we use a grating with 1200 lines/mm, giving a Voigt line shape instrument function with a full-width at half maximum linewidth of 1.8 cm^{-1} for the Gaussian component and 1.6264 cm^{-1} for the Lorentzian component at about 600 nm, corresponding to the Stokes vibrational Raman feature of N_2 at around 2100 to 2400 cm^{-1} .

The spectral fitting routine for temperature determination is performed with an in-house Python code. The equations given below are adapted and follow the nomenclature from [33] with references given where modifications are made. For fitting the rotational and vibrational

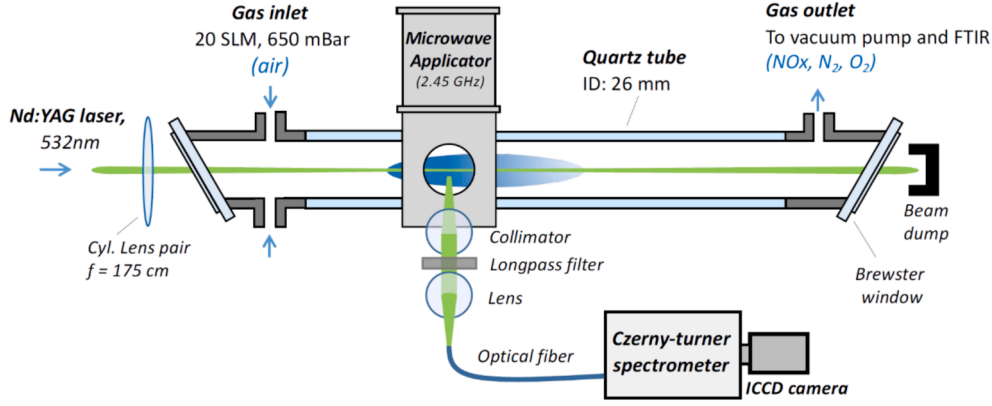


Fig. 1. Reactor setup and laser alignment for in-situ Raman spectroscopy.

temperature from the N_2 vibrational Raman spectrum, we need only to consider only Q branch ($\Delta J = 0$) transitions of the first vibrational Stokes branch ($\Delta \nu = +1$). For Raman scattering, the total energy of a diatomic molecule can be expressed as the sum of its rotational (E_r) and vibrational energy (E_v):

$$E = E_r(\nu, J) + E_v(\nu) \quad (1)$$

where the rotational energy term is a function of the total rotational (J) and vibrational (ν) quantum numbers of the molecule, and is expressed by:

$$E_r(\nu, J) = B_\nu J(J+1) - D_\nu J^2(J+1)^2 \quad (2)$$

where B_ν is the rotational constant for a given vibrational state and D_ν is the centrifugal distortion constant. Higher-order terms for centrifugal distortion are incorporated in our script but do not need to be considered for the Q-branch vibrational transitions.

The rotational constant is calculated with:

$$B_\nu(\nu) = B_e - \alpha_e \left(\nu + \frac{1}{2} \right) \quad (3)$$

B_e is the rotational constant at equilibrium internuclear separation and α_e is the first-order anharmonicity correction for the rotational constant. We do not include higher-order terms for the anharmonicity constant.

The first centrifugal distortion constant is given by:

$$D_\nu(\nu) = D_e - \beta_e \left(\nu + \frac{1}{2} \right) \quad (4)$$

D_e is the centrifugal distortion constant at equilibrium internuclear separation and β_e is the first-order anharmonicity correction for the centrifugal distortion constant.

The vibrational energy term is given by:

$$E_v(\nu) = \left(\nu + \frac{1}{2} \right) w_e - w_e x_e \left(\nu + \frac{1}{2} \right)^2 \quad (5)$$

where w_e is the harmonic vibration wavenumber and $w_e x_e$ is the vibrational anharmonicity constant. The line positions of the Raman transitions are determined by the energy difference between the lower and upper rovibrational states:

$$\Delta E = E'(\nu, J) - E''(\nu, J) \quad (6)$$

For fitting the spectra to determine temperature, it is required only to know the relative intensities of the spectral lines. In general, the relative intensities of Stokes Raman transitions are given by:

$$I \propto \tilde{\nu}_s^4 N_i \Phi(a^2, \gamma^2, \theta) \quad (7)$$

where $\tilde{\nu}_s$ is the frequency of scattered radiation in wavenumbers, equivalent to ΔE given above, N_i is the population density of the molecules in an initial rovibrational state, and $\langle (\alpha)_{fi}^2 \rangle$ is the squared isotropic average of the transition polarizability.

The population density is assumed to follow a Boltzmann distribution in both rotational and vibrational populations, an assumption we have observed to be valid for these experiments. The population density in a rovibrational state is expressed by:

$$N_i = N_{tot} \frac{g_v}{Q_v} \frac{g_r}{Q_r} \exp \left[-\frac{hc}{k_b} \left(\frac{\tilde{E}_v}{T_v} + \frac{\tilde{E}_r}{T_r} \right) \right] \quad (8)$$

Several terms are constant for all Raman transitions and can therefore be neglected in the calculation of relative intensities. These constant terms are as follows: N_{tot} is the gas density determined by the ideal gas law, Q_v and Q_r are the vibrational and rotational partition functions. The vibrational degeneracy g_v for a diatomic molecule is 1, whilst the rotational degeneracy is given by $g_r = 2J + 1$, and nuclear spin degeneracy for N_2 alternates for odd and even values of J and, h , c , and k_b are the Planck constant, speed of light, and Boltzmann constant, respectively. \tilde{E}_v and \tilde{E}_r are the lower state vibrational and rotational energies, expressed in wavenumbers. Likewise, T_v and T_r are the vibrational and rotational temperatures.

The function $\Phi(a^2, \gamma^2, \theta)$ is obtained from the squared isotropic average of the transition polarizability tensor, $\langle (\alpha)_{fi}^2 \rangle$, for a $\Delta \nu = +1, \Delta J = 0$ transition including both the perpendicular and parallel components of the scattered radiation. This is given by:

$$\Phi(a^2, \gamma^2, \theta) = (a')^2 F_a(J) + \frac{7}{45} b_{J,J'}^2 (\gamma')^2 F_\gamma(J) \quad (9)$$

The mean and anisotropic invariants of the derived polarizability tensor are expressed by a' and γ' . $F_a(J)$ and $F_\gamma(J)$ are the Herman-Wallis factors, which compensate for vibration-rotation coupling. For both the polarisabilities and the Herman-Wallis factors, we use the method and constants given by Buldakov, et al. [34]. Note that the scaling of intensities with ν by a factor $(\nu + 1)$ is incorporated in the polarizability term. The terms $b_{J,J'}$ are the Placzek-Teller coefficients, which for the Q-branch ($\Delta J = 0$) are given by:

$$b_{J,J} = \frac{J(J+1)}{(2J-1)(2J+3)} \quad (10)$$

The spectroscopic constants used in the calculation of the N_2 Raman spectrum are given in Table 1.

Experimental results show no significant influence of vibrational excitation at any of the 24 positions measured within the plasma reactor as shown in Fig. 2.

Table 1
Spectroscopic data used for fitting the Raman spectrum of N₂.

Constant	Value	Reference
w_e	2358.62 cm ⁻¹	[35]
$w_e x_e$	14.3444 cm ⁻¹	[35,36]
B_e	1.99829 cm ⁻¹	[35,37]
α_e	1.74130 × 10 ⁻² cm ⁻¹	[35,37]
D_e	5.49723 × 10 ⁻⁶ cm ⁻¹	[35]
β_e	-7.67491 × 10 ⁻⁸ cm ⁻¹	[35]
$g_n(\text{Odd } J)$	3	[38]
$g_n(\text{Even } J)$	6	[38]

3. Numerical modeling methodology

3.1. Flow and energy governing equations

Flows characterized by low Reynolds number imply laminar flow conditions for which the continuity equation of the mixture is given by Eq. (11):

$$\frac{\partial \rho}{\partial t} + \nabla \cdot (\rho \vec{V}) = 0 \quad (11)$$

The conservation of each chemical species is governed by the associated transport equation given by Eq. (12):

$$\frac{\partial (\rho m_i)}{\partial t} + \nabla \cdot (\rho \vec{V} m_i) + \nabla \cdot \vec{J}_i = R_i \quad (12)$$

The momentum of the mixture gas is described by the Navier-Stokes equations given by (13):

$$\frac{\partial (\rho \vec{V})}{\partial t} + \nabla \cdot (\rho \vec{V} \vec{V}) + \nabla p = \nabla \cdot \vec{\tau} \quad (13)$$

Here $\vec{\tau}$ is the tensor of shear stress imposed on fluid element computed by Eq. (14):

$$\vec{\tau} = \mu \left[(\nabla \vec{V} + \nabla \vec{V}^T) - \frac{2}{3} \nabla \cdot \vec{V} I \right] \quad (14)$$

The total energy of a fluid volume is described by Eq. (15):

$$\frac{\partial (\rho E)}{\partial t} + \nabla \cdot (\vec{V} (\rho E + p)) = \nabla \cdot \left[\lambda \nabla T - \sum_i h_i \vec{J}_i + (\vec{\tau} \cdot \vec{V}) \right] \quad (15)$$

In Eq. (15), E denotes the general formulation for the sum of enthalpy, static and kinetic energy of the fluid element given by Eq. (16):

$$E = h - \frac{p}{\rho} + \frac{|\vec{V}|^2}{2} \quad (16)$$

In Eq. (16), the total enthalpy of the mixture, h , is the weighted-averaged of each chemical species enthalpy calculated by Eq. (17):

$$h = \sum m_j h_j \quad (17)$$

Here h_j is the sensible enthalpy of species and is part of the enthalpy that includes only changes due to specific heat, computed by Eq. (18):

$$h_j = \int_{T_{ref}}^T C_{p,j} dT + h_{0,j} \quad (18)$$

3.2. Chemical non-equilibrium reaction modeling

To compute the source term in Eq. (12) for each species, the laminar finite-rate model was adopted using the Arrhenius expressions which ignore the effects of turbulence on the chemistry rates and is valid for all laminar flows and those turbulent ones where the interaction is negligible. Reactions were considered as non-equilibrium reversible formulation where the forward rate constant for reaction r is computed by Eq. (19):

$$k_{f,r} = A_r T^{\beta_r} \exp \left[- \left(\frac{E_r}{RT} \right) \right] \quad (19)$$

In Eq. (19) A_r , β_r and E_r are the pre-exponential factor, temperature exponent, and activation energy of each reaction, respectively and R is the universal gas constant. The backward rate constant is calculated by Eq. (20):

$$k_{b,r} = \frac{k_{f,r}}{K_r} \quad (20)$$

K_r is the equilibrium constant for each reaction and is computed as a function of Gibbs free energy.

A five-species air model (N₂, O₂, NO, N, O) proposed by Park [39] was used to model the chemistry in this study, shown in Table 2 where M_{mol} represents N₂, O₂, and NO molecules and M_{atom} denotes N and O

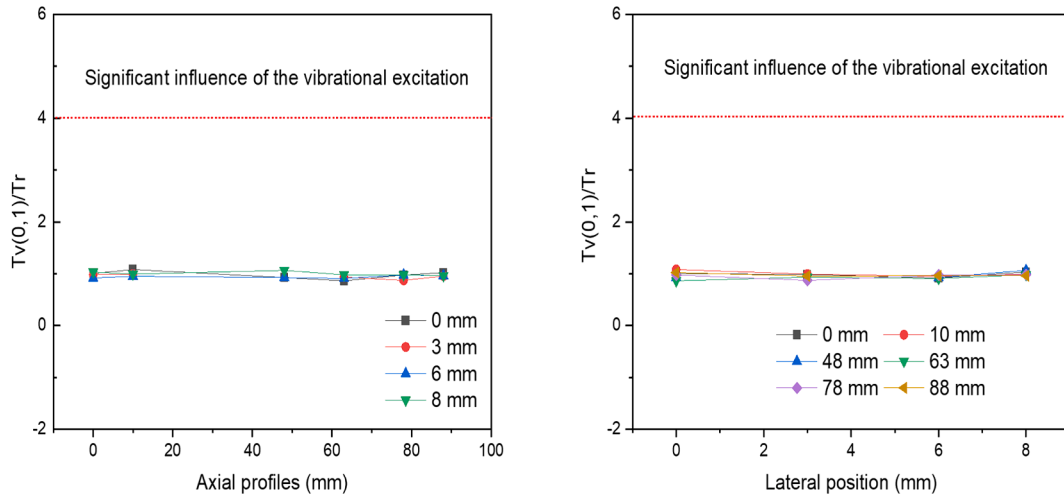


Fig. 2. Summary of temperature measurements within the plasma reactor.

atoms. Due to the level of operating pressure in this work, the vibrational and rotational temperatures of the gas are very close to each other. Thus, the use of such a chemical kinetic scheme is valid.

3.3. Transport properties

All transport properties of individual species are computed based on kinetic theory. The fluid viscosity of each chemical species is defined in Eq. (21):

$$\mu_i = 2.67 \times 10^{-6} \frac{\sqrt{M_i T}}{\sigma_i^2 \Omega_{\mu i}} \quad (21)$$

where M_i is the molar weight of each species and σ_i and $\Omega_{\mu i}$ are the corresponding Lennard-Jones parameter and the diffusion collision integral.

The thermal conductivity of each species is computed by Eq. (22):

$$\lambda_i = \frac{15}{4} \frac{R}{M_i} \mu_i \left[\frac{4}{15} \frac{C_{pi} M_i}{R} + \frac{1}{3} \right] \quad (22)$$

where μ_i and C_{pi} are the viscosity and specific heat of the chemical species.

The binary mass diffusion coefficient is calculated using Eq. (23):

$$D_{ij} = 0.00188 \frac{\left[T^3 \left(\frac{1}{M_i} + \frac{1}{M_j} \right) \right]^{0.5}}{p_{abs} \sigma_{ij}^2 \Omega_{Dij}} \quad (23)$$

where p_{abs} is the absolute pressure of the fluid element, and the associated kinetic theory parameters were exploited from [40].

The mass diffusion coefficient of species i in the mixture is then calculated following Eq. (24):

$$D_{im} = \frac{1 - X_i}{\sum_j (X_j / D_{ij})} \quad (24)$$

where X_i is the mole fraction of species i .

A mixing law formulation is utilized for the computation of the mixture viscosity as in Eq. (25):

$$\mu = \sum_i \frac{X_i \mu_i}{\sum_j X_j \phi_{ij}} \quad (25)$$

where the function ϕ_{ij} is defined by Eq. (26):

$$\phi_{ij} = \frac{\left[1 + \left(\frac{\mu_i}{\mu_j} \right)^{0.5} \left(\frac{M_{wi}}{M_{wj}} \right)^{0.25} \right]^2}{\left[8 \left(1 + \frac{M_{wi}}{M_{wj}} \right) \right]^{0.5}} \quad (26)$$

The same formulation was used for the thermal conductivity of the mixture given by Eq. (27):

$$\lambda = \sum_i \frac{X_i \lambda_i}{\sum_j X_j \phi_{ij}} \quad (27)$$

3.4. Thermodynamic model

This study treats the flow as a warm plasma, based on the Raman spectroscopy results that showed no evidence of vibrational-rotational non-equilibrium. Therefore, the assumption of one distinguished temperature in the numerical domain was made. In this approach, the thermal relaxation time is much smaller than the characteristic time of fluid motion. This is a valid assumption for operating pressure levels in the order of high subatmospheric and atmospheric conditions where the vibrational and translation-rotation temperature levels are almost the same. An assessment of the vibrational non-equilibrium relaxation time in N_2 is done by Van de Steeg, et al. [32]. The ideal gas law is used for each species as defined by Eq. (28):

$$p_i = \rho_i R_i T \quad (28)$$

where the total pressure is computed given by Eq. (29):

$$p = \sum_i p_i \quad (29)$$

The specific heat of each species is defined as a polynomial function of temperature [41] and a mass fraction-averaged relation is used for computation of the mixture specific heat given by:

$$C_p = \sum_i X_i C_{pi} \quad (30)$$

3.5. Boundary condition and numerical scheme

The boundaries of the plasma reactor are influenced by radiative and convective heat losses. The model balances the convective heat flux on the inside with the conductive heat flux through the reactor wall, and the external heat losses due to convection and radiation under steady-state operation. The local outer reactor wall temperature is used to determine the local heat transfer coefficient for free convection, using classical Nusselt number correlation [42], and to calculate the local radiative heat loss. The model is closed by specifying the reactor wall thickness, wall thermal conductivity, and wall emissivity. In this way, local heat losses are obtained on all exterior nodes on the reactor boundary.

Solving a fully coupled model based on the fluid dynamic and electromagnetic governing equations is not feasible at high pressures even on the largest computer clusters for the foreseeable future. Hence, the shape and size of the microwave heat source were obtained by analyzing auto-exposed images of the reactor core and relating the local light intensity with the local ionization. The auto-exposed images contain information about the size and shape of the ionized region, particularly the blue channel shows a well-defined boundary as shown in Fig. 3. The heat source was defined as homogenous power absorption per unit volume within the region defined by the boundary. This region corresponds to a maximum radius of 2.4 mm, which means that one of the measurement lines used for validation falls within the boundary while the other measurement lines are located between the core and the reactor wall, thereby covering the critical region for validating the temperature profile inside the reactor.

Numerical strategies were investigated to allow converged simulations and optimize the computational time. It was found that a coupled solver is required to solve the couple set of partial differential equations, due to the strong interaction between the flow, temperature, and species fields. In addition, the CFD solver gained from ramping up the microwave power source and the Courant number during iterations to reach steady state condition.

Table 2
Chemical reactions used in the CFD simulation.

Reactions	$A_r \left(\frac{cm^3}{mole.s} \right)$	β	E_r/R
$N_2 + M \leftrightarrow N + N + M$	$M=M_{mol}: 7.0 \times 10^{21}$	-1.6	113200
	$M=M_{atom}: 3.0 \times 10^{22}$	-1.6	
$O_2 + M \leftrightarrow O + O + M$	$M=M_{mol}: 2.0 \times 10^{21}$	-1.5	59500
	$M=M_{atom}: 1.0 \times 10^{22}$	-1.5	
$NO + M \leftrightarrow N + O + M$	$M=M_{mol}: 5.0 \times 10^{15}$	0.0	75500
	$M=M_{atom}: 1.1 \times 10^{17}$	0.0	
$N_2 + O \leftrightarrow NO + N$	6.4×10^{17}	-1.0	38400
$NO + O \leftrightarrow O_2 + N$	8.4×10^{12}	0.0	19450

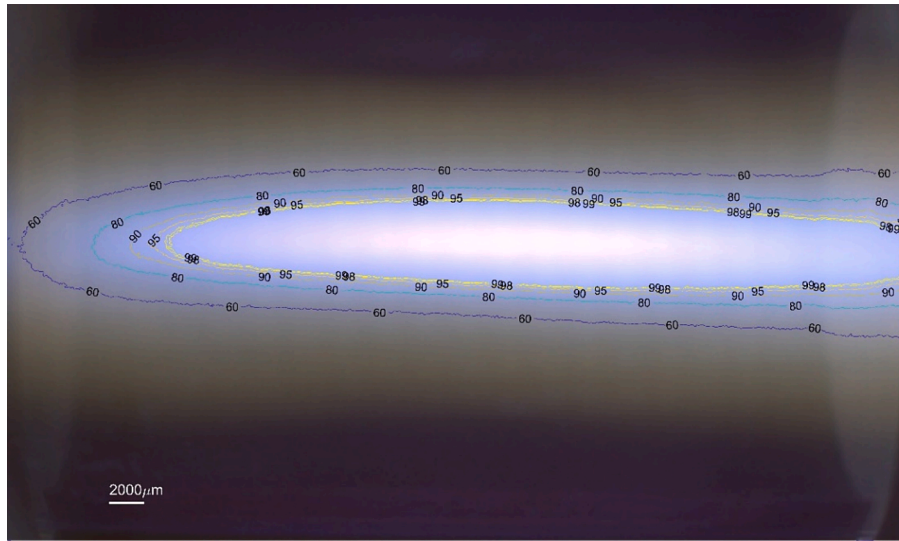


Fig. 3. Microwave air plasma discharge superposed by iso-lines of light intensity.

3.6. Analysis of mesh independence

Following best practices in CFD modeling, the mesh was refined in bulk and in the regions with large gradients of the solution variables to

ensure mesh-independent results [43]. Mesh independence was achieved at 6.2 million cells by using gradient adaptation on the species, velocity, and temperature fields. Results from the mesh independence analysis are shown in Fig. 4 and summarized in Table 3. Here the

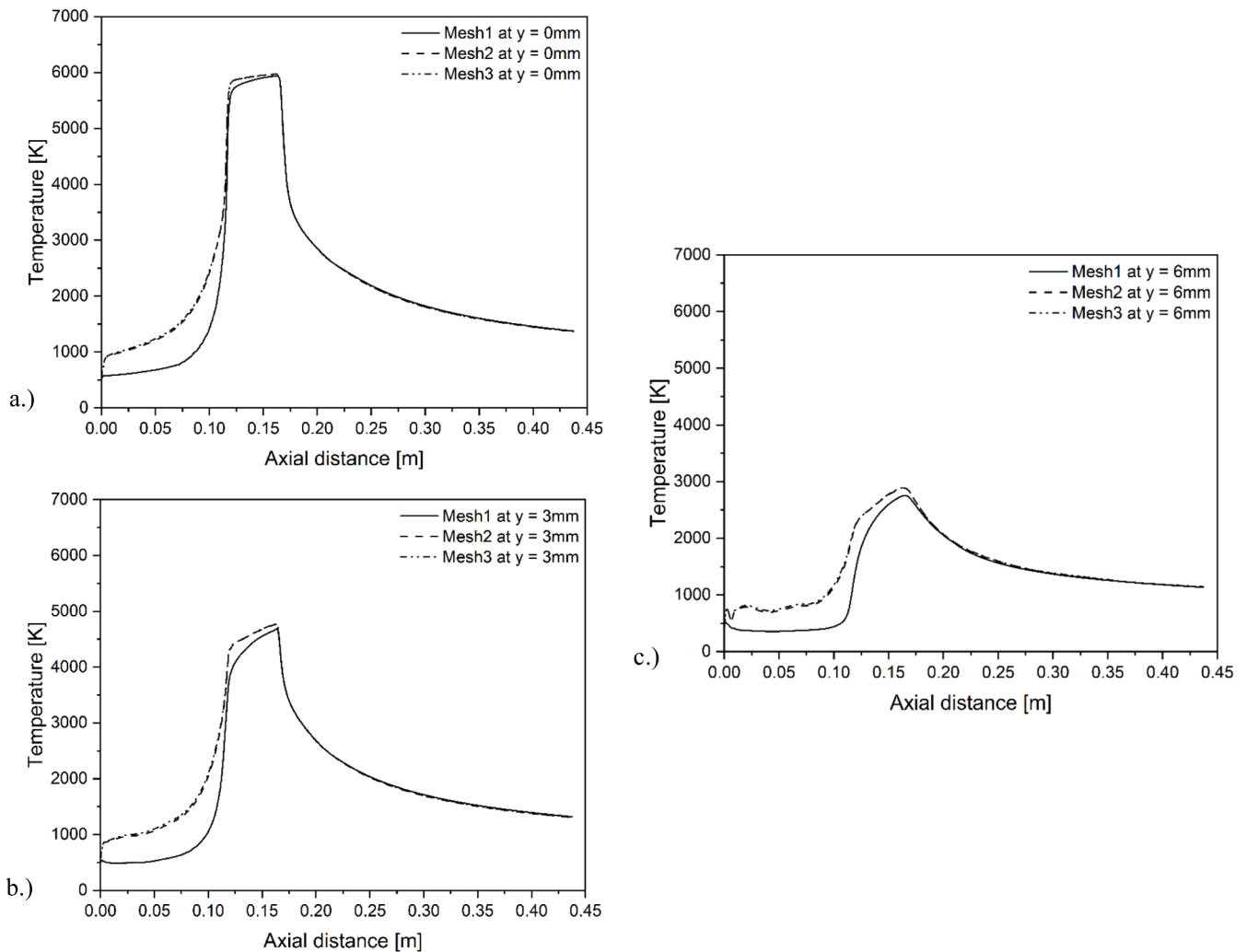


Fig. 4. Mesh independence analysis. Temperature profiles at different distances from the reactor core a.) $y = 0$ [mm], b.) $y = 3$ [mm], and c.) $y = 6$ [mm].

Table 3
Summary of the mesh independence analysis.

	Mesh 1	Mesh2	Mesh3
Cells	579,147	6,245,968	7,450,557
Maximum temperature	5943	5972	5972
Mole fraction NO (%)	0.755	0.743	0.743

reported mole fraction is calculated using the mass flow weighted average at the reactor outlet defined by Eq. (32). All simulation results in the subsequent sections are based on the mesh-independent model.

4. Results, validation and discussion

4.1. Flow field analysis

Investigation of the three-dimensional flow field shows distinctive characteristics within the reactor, distinguishing it from the flow patterns observed in conventional tubular reactors. These notable features include the occurrence of reverse flow in the initial segment of the reactor, the establishment of a stagnation point along the axial direction at approximately one-fourth of the distance from the inlet, and the presence of regions featuring accelerated flow, which later transitions into an increasingly parabolic flow profile closer to the reactor outlet as depicted in Fig. 5. Compared to the characteristic parabolic flow profile for a fully developed laminar pipe flow, the profile at the reactor outlet is slightly more flattened since the viscous momentum transport has limited time to act before the gas exits the reactor. Result shows that the ratio $V_{max}/V_{mean} = 1.846$ at the reactor outlet which corresponds to 92.3 % recovery of the value for a fully developed laminar pipe flow for which $V_{max}/V_{mean} = 2$. For the sake of clarity, Fig. 5 shows the flow profiles at four specified lines downstream of the reactor instead of displaying all vectors, and the aspect ratio in the plot is adapted to improve the clarity of the flow details.

The reverse flow and the establishment of a stagnation point, as illustrated in Fig. 5a (Line1 and Line2, respectively), are explained by the synergistic impact of the pressure field and the gas expansion resulting from the heating of the gas by the plasma and the

corresponding molar change due to gas dissociation which occurs at sufficiently high temperature. The static pressure field distribution relative to the operating pressure is shown in Fig. 6.

Since gas expansion occurs in all directions the gas can flow backward towards the inlet in the upstream section of the reactor. In contrast, in the downstream section of the reactor the gas expansion acts in the same direction as the bulk flow and leads to an accelerated flow in the core towards the reactor outlet as shown in Fig. 5a (Line3). Simultaneously viscous momentum transfer continuously acts on all fluid elements in the reactor to revert the flow profile towards the classical flow profile in tubular reactors, as evident from the flow profile that is established in Fig. 5a (Line4).

As expected, the swirling flow is established directly at the inlet due to the tangentially placed gas inlets, which is illustrated by streamlines colored by the velocity magnitude in Fig. 5b. Clearly the swirling flow, although moderately weakened, survives throughout the reactor which allows the tangential cold flow to surround the hot core. Weakening of the swirling flow is expected since the gas viscosity increases at higher temperatures and the no-slip condition acts at the reactor wall. The centrifugal force keeps the cold gas flowing along the walls and the hot core in the center, which prevents the reactor wall from overheating although the core reaches a very high temperature.

Considering the complexity of the flow it is of interest to analyze the residence time distribution (RTD) to understand the overall effect of hydrodynamic dispersion in the reactor. The combined effect of the different flow features is characterized by a numerical step response analysis of an inert tracer at the inlet and a measure at the reactor outlet. This allows the RTD to be calculated by differentiating the normalized outlet step response signal using Eq. (31):

$$E(t) = \frac{d}{dt} \left[\frac{C_{out}(t)}{C_0} \right]_{step} \quad (31)$$

The resulting RTD curve, calculated by Eq. (31), characterizes the overall effect of hydrodynamic dispersion within the reactor and is shown in Fig. 7. From this, it is concluded that the mean residence time in the reactor equals $\bar{t} = \int_0^\infty tE(t)dt = 0.116$ s. As evident from the variance and skewness of the RTD, the hydrodynamics inside the reactor

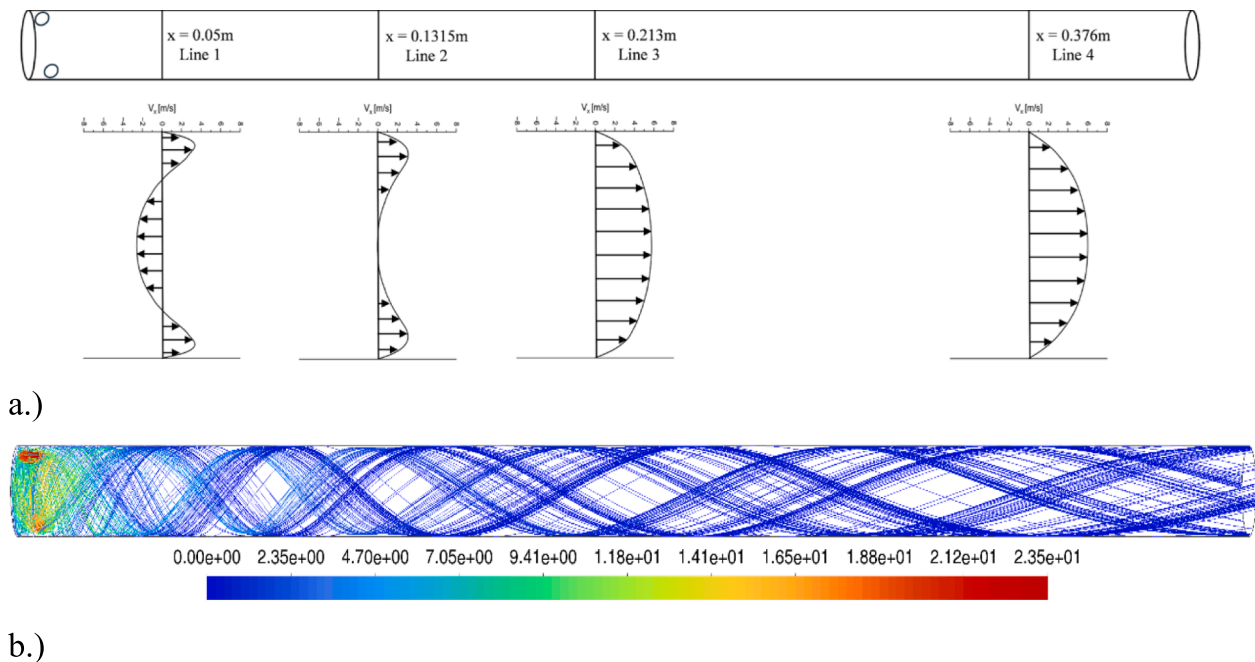


Fig. 5. a.) Velocity component, V_x , illustrating the characteristic flow features at four different cross-sectional lines, b.) Velocity streamlines colored by the velocity magnitude, both figures have the unit [m/s].

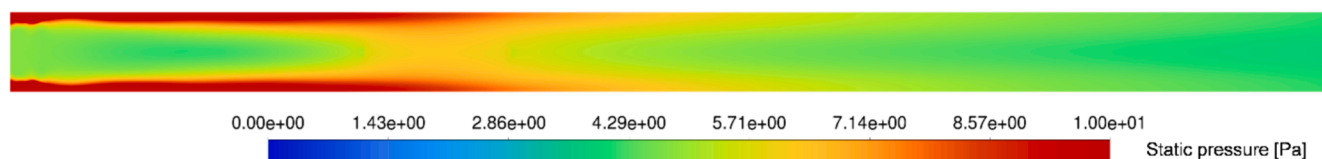


Fig. 6. Static pressure distribution relative to operating pressure.

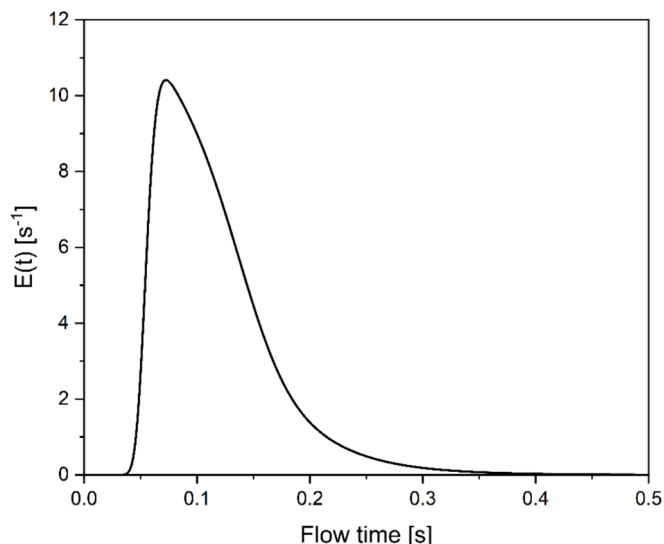


Fig. 7. Residence time distribution, $E(t)$, obtained from a numerical step analysis.

is far from an ideal flow.

Considering the significant hydrodynamic dispersion and the large radial temperature gradients inside the reactor (as discussed in the next section), it seems not possible to formulate a simplified reactor model. A one-dimensional tubular reactor model with dispersion is not considered as an alternative modeling approach. Instead, the coupling between transport phenomena and chemical reactions must be accounted for by using a three three-dimensional model to provide reliable results.

4.2. Temperature and species distribution

Validation of the temperature profile throughout the reactor by use of in-situ Raman spectroscopy shows a good agreement with simulations. The axial temperature profiles, defined by discrete measurement points on the symmetry axis and at distances 3 mm and 6 mm away from the symmetry axis, are shown in Fig. 8. The highest temperature exists in the core as expected and reaches close to 6000 K. Fig. 9 shows a cross-section contour plot of the temperature distribution throughout the reactor. Notably, there are no large gradients within the core where the temperature is between 5000 to 6000 K, but significant radial and axial temperature gradients are found outside this region. Due to the backward flow in the upstream region of the reactor (discussed in the previous section), a region with moderate temperature develops in the reactor due to the convective transport of gas that occurs along the center but in the opposite direction compared to the outer flow which flows towards the outlet.

In addition, results from the wall temperature measurement are included in Fig. 8, to provide an overview of the large temperature range that exists inside the domain. Although the reactor wall temperature increases slightly in the axial direction the wall temperature remains low in general and poses no problem to maintain the integrity of the reactor wall. Given the broad range of temperature variations within the system, the simulations are deemed to offer highly accurate predictions.

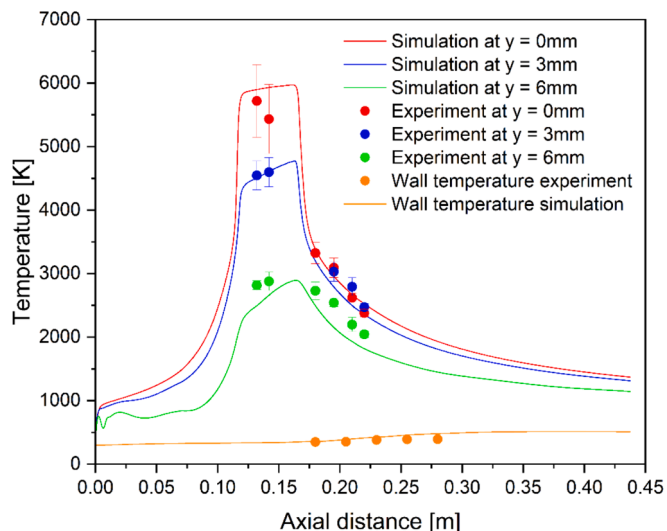


Fig. 8. Validation of gas and wall temperatures at different axial and radial locations inside the reactor.

The radial temperature gradient, in particular, plays a crucial role in explaining the reactor's functions. Both experiments and simulations consistently show that temperature gradients of up to 700 K per millimeter are established during steady operation in the outer part of the core, as shown in Fig. 9. Resolving the sharp gradient is crucial for a model to accurately represent the reactor's functionalities, as it is closely related to the net formation of species. This is further discussed in the next section.

The species distribution inside the reactor develops as an effect of the flow field, temperature field, and local chemical reactions. Simulations reveal that the reactor includes regions that are dominated by forward chemical reactions, while other regions are dominated by backward chemical reactions. As a result, the variation in the molar fraction throughout the reactor becomes significant. Fig. 10 shows a cross-section contour plot of the species distribution from which is readily seen that a local minimum is formed in the core. This is expected due to the instability of the bond in the NO molecule at the highest temperature. It is also clear that the model predicts a maximum molar fraction equal to 4.56 % at 3500 K, which is close to the equilibrium composition calculated by the minimization of Gibbs free energy which equals 4.88 % for gas mixtures of 21 % O_2 and 79 % N_2 at this temperature and pressure of 0.65 bar. The temperature in the middle of the hot core exceeds by far the optimal temperature and the composition is reduced to 0.69 % mole. This is also consistent with Gibbs free energy calculation which yields an equilibrium composition of 0.68 % mole at 5900 K and 0.65 bar.

The net NO formation exiting the reactor is characterized by the mass flow weighted average that is calculated by accounting for the local molar fraction, y , density, ρ , and flow field distribution, \vec{V} , at the reactor outlet, i.e. mixed-cup average, defined by Eq. (32). This allows direct comparison between the CFD simulations and the FTIR measurement.

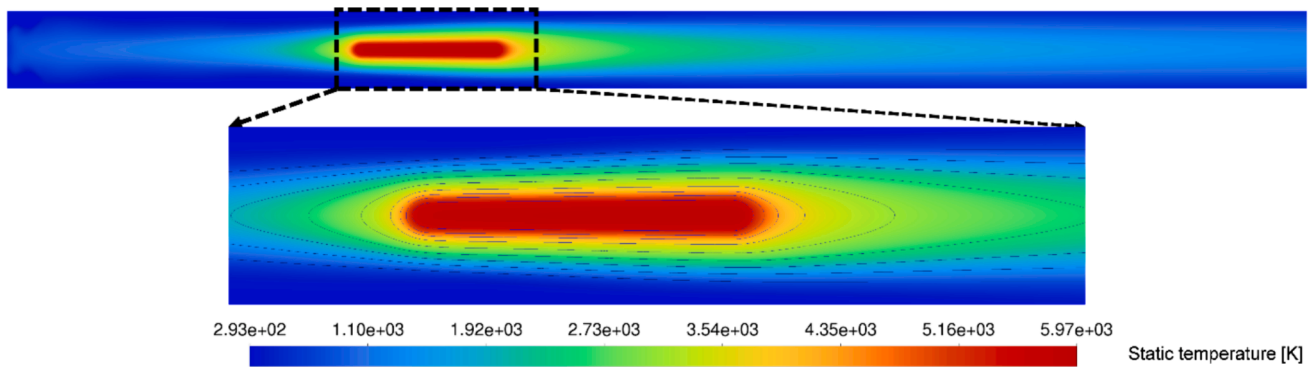


Fig. 9. Temperature distribution in a cross-sectional plane in the middle of the reactor.

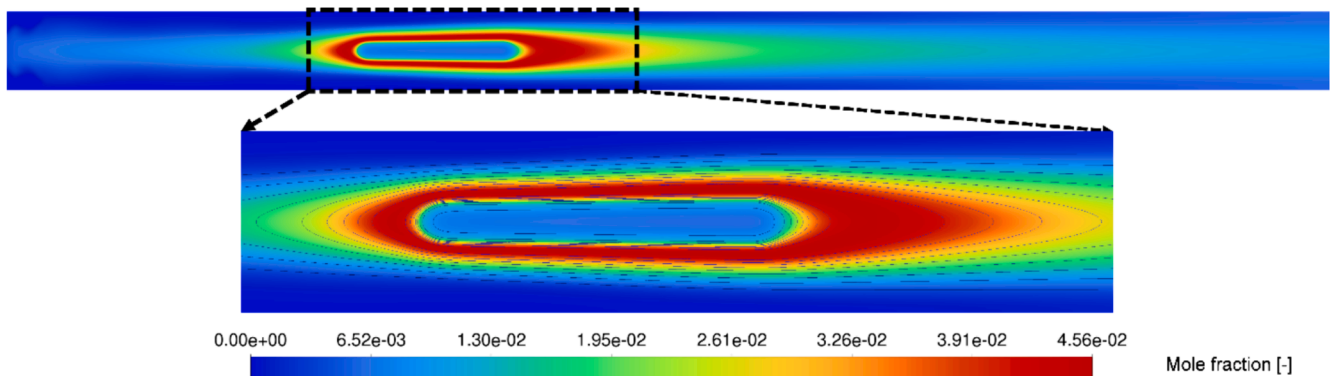


Fig. 10. NO mole fraction distribution in a cross-sectional plane in the middle of the reactor.

$$\bar{y} = \frac{\int y \rho |\vec{V} \cdot d\vec{A}|}{\int \rho |\vec{V} \cdot d\vec{A}|} \quad (32)$$

Results are summarized in Table 4, which confirms good agreement between simulations and experiments.

A comparison between CFD simulations and experiments for a range of different power inputs, 200 to 700 W, provides additional evidence that the model accurately predicts nitrogen fixation. Overall, the results agree very well and show a clear linear correlation between power input and NO_x concentration as summarized in Fig. 11.

4.3. Chemical reactions and intrinsic quenching

Analysis of the simulation results reveals that regions dominated by forward and backward reactions are largely localized in the middle of the reactor. Nitrogen fixation occurs primarily in a hollow ellipsoidal region as shown in Fig. 12. While high temperatures are favorable condition to form nitrogen oxides, the center part of the hot core region provides conditions where the molecular bonds are not sufficiently strong to keep the molecules together, which leads to net destruction. The region dominated by backward reactions is identified as the red region in Fig. 12. Conversely, the reactor provides favorable conditions in a hollow ellipsoidal region (blue region), as shown in Fig. 12. By a gradient-driven transport, emanating from high-concentration regions, species are transported outwards towards the surrounding flow thereby

Table 4

Comparison between simulation and experimental results at 400 W power input.

	Experiment	Simulation
Power input (absorbed)	400	400.9
Mole fraction NO (%)	0.740	0.743

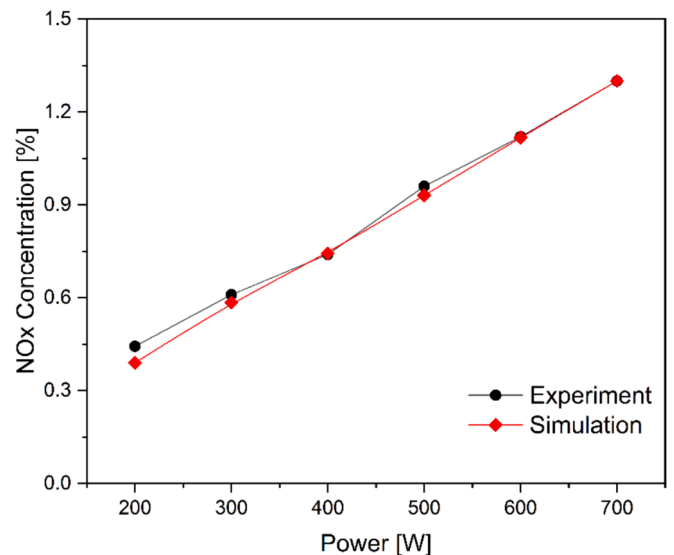


Fig. 11. Comparison between measured and simulated NO_x concentration at the reactor outlet as a function of the power input.

enriching the bulk concentration.

A clearer view of the regions having net formation and net destruction is obtained by separating the positive and negative values, as shown in Fig. 13a and b, respectively.

Simulation shows that the outward-directed species transport occurs via a region having a large temperature gradient which allows the preservation of a significant portion of the nitrogen oxide. The temperature gradient in this region is observed to be close to 700 K per

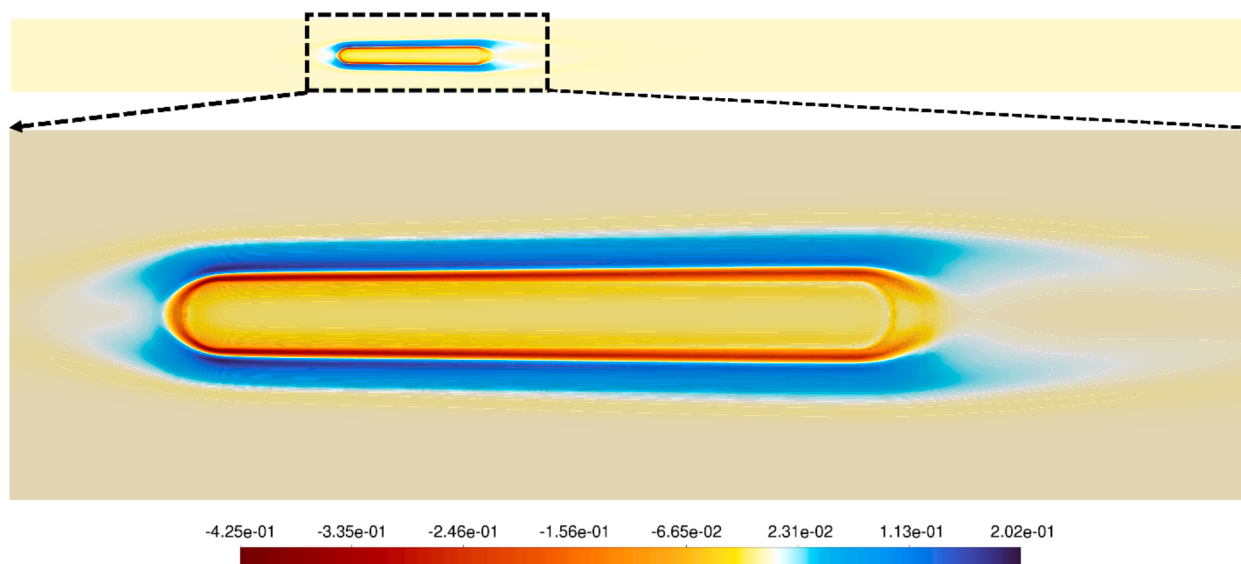
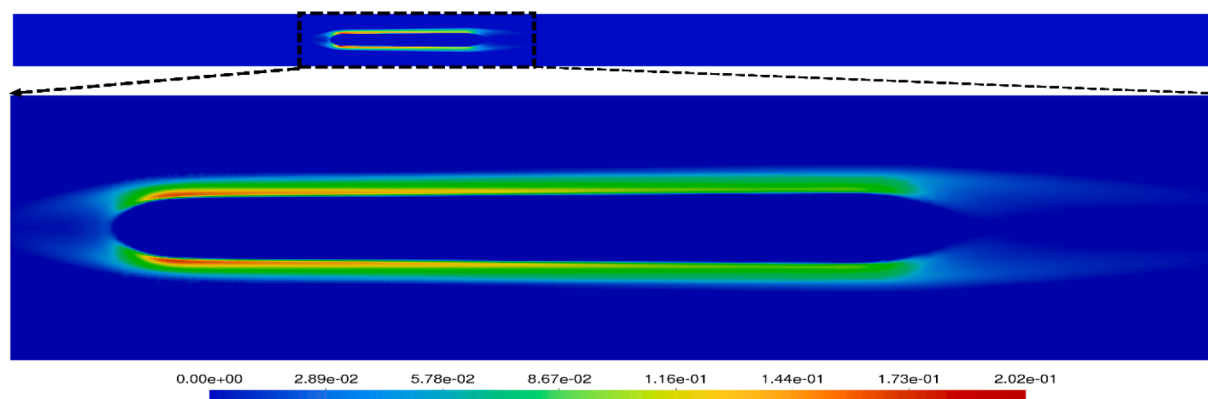
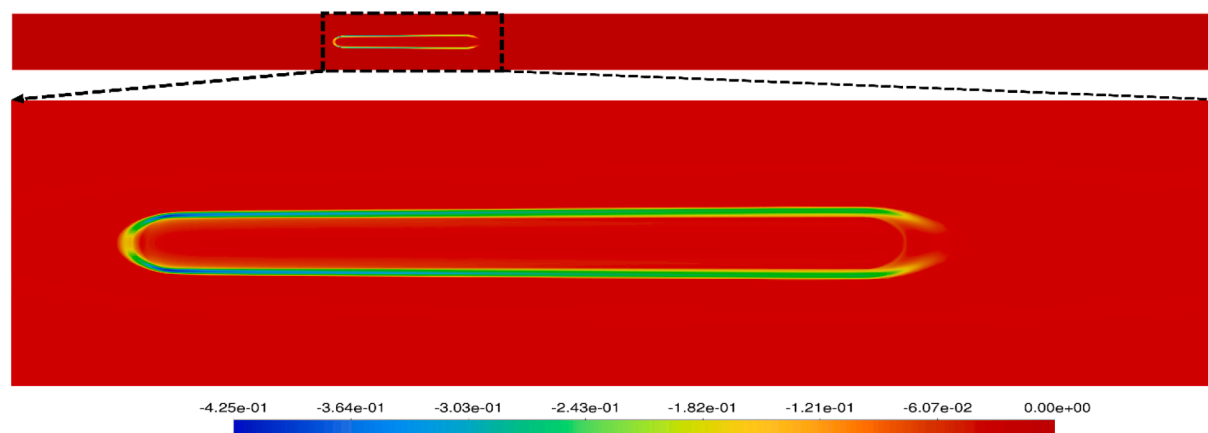


Fig. 12. Net NO formation rate in a cross-sectional plane in the middle of the reactor.



a.)



b.)

Fig. 13. Regions with a.) net NO formation, and b.) net NO destruction.

millimeter. In other words, the temperature field works to preserve the species by intrinsic quenching. Alternative reactor designs allowing steeper temperature gradients have the potential to enhance the efficiency of the intrinsic quenching further and thereby to allow higher yield.

5. Conclusions

This study combines state-of-the-art in-situ measurements and advanced 3D simulations to diagnose and understand the operation of a plasma reactor at high subatmospheric pressure under various power

inputs. Overall, calculations and measurements agree very well, including temperature profiles inside the reactor, wall temperatures, and reactor yield at different power inputs. Results show that the reactor can be described as a warm plasma based on the negligible differences observed in vibrational and rotational temperatures. Additionally, a complex flow field and significant temperature and concentration gradients within the reactor were identified. These findings underscore the necessity of using 3D simulations to accurately describe the interplay between mass, heat, and momentum transport and the chemical reactions occurring in non-equilibrium conditions. The flow field is characterized by an outer rotating region with a low temperature, which stabilizes the plasma core through centrifugal forces acting on the fluid due to substantial density variations across the cross-section, while efficiently cooling the reactor walls. The innermost region of the plasma reaches a temperature close to 6000 K, yet low reactor wall temperatures are maintained, consistent with the measurements. The inner part of the flow features a recirculation zone, a stagnation point, and a gradual return to a parabolic flow profile closer to the reactor outlet. Regions dominated by reactant decomposition and product formation occur at the expected temperature levels. Local concentrations at high temperatures match those predicted by equilibrium calculations at respective temperatures, peaking in the reactor center as anticipated. Meanwhile, substantial radial temperature gradients partially freeze the concentrations, preventing a return to equilibrium at lower temperatures through continuous gradient-driven transport of molecules perpendicular to the main flow direction. Collaboration between groups specializing in plasma physics and reaction engineering calculations proves advantageous, yielding new insights into the coupling between transport phenomena and chemical non-equilibrium reactions in a complex 3D flow field. Validated 3D simulations from this study open possibilities for exploring alternative and improved reactor designs with higher yields through modeling, potentially increasing interest in plasma technology as part of the electrification of chemical processes.

CRedit authorship contribution statement

Massoud Tatar: Writing – review & editing, Writing – original draft, Validation, Software, Investigation, Formal analysis. **Vikash Vashisth:** Writing – original draft, Visualization, Software, Investigation, Formal analysis. **Muzammil Iqbal:** Writing – original draft, Validation, Investigation, Formal analysis. **Thomas Butterworth:** Writing – review & editing, Writing – original draft, Supervision, Investigation. **Gerard van Rooij:** Writing – review & editing, Supervision, Project administration, Methodology. **Ronnie Andersson:** Writing – review & editing, Supervision, Project administration, Methodology, Funding acquisition, Conceptualization.

Declaration of competing interest

The authors declare that they have no known competing financial interests or personal relationships that could have appeared to influence the work reported in this paper.

Data availability

Data will be made available on request.

Acknowledgments

Financial support from the Swedish Energy Agency (Grant: 2021-037459) is gratefully acknowledged. The computations were enabled by resources provided by the National Academic Infrastructure for Supercomputing in Sweden (NAISS) at Chalmers e-Commons/C3SE partially funded by the Swedish Research Council through grant agreement no. 2022-06725.

References

- [1] N. Cherkasov, A. Ibhaden, P. Fitzpatrick, A review of the existing and alternative methods for greener nitrogen fixation, *Chem. Eng. Process.* 90 (2015) 24–33.
- [2] J. Liu, L. Nie, D. Liu, and X. Lu, "Plasma for nitrogen fixation by using N₂/O₂ mixture: Reaction pathway, energy flow, and plasma reactor," *Plasma Processes and Polymers*, p. e2300153.
- [3] B. Patil, Q. Wang, V. Hessel, J. Lang, Plasma N₂-fixation: 1900–2014, *Catal. Today* 256 (2015) 49–66.
- [4] K.H. Rouwenhorst, F. Jardali, A. Bogaerts, L. Lefferts, From the Birkeland-Eyde process towards energy-efficient plasma-based NO_x synthesis: a techno-economic analysis, *Energ. Environ. Sci.* 14 (2021) 2520–2534.
- [5] X. Pei, D. Gidon, Y.-J. Yang, Z. Xiong, D.B. Graves, Reducing energy cost of NO_x production in air plasmas, *Chem. Eng. J.* 362 (2019) 217–228.
- [6] V. Cooray, M. Rahman, V. Rakov, On the NO_x production by laboratory electrical discharges and lightning, *J. Atmos. Sol. Terr. Phys.* 71 (2009) 1877–1889.
- [7] S. Van Alphen, H.A. Eshtehardi, C. O'Modhrain, J. Bogaerts, H. Van Poyer, J. Creel, et al., Effusion nozzle for energy-efficient NO_x production in a rotating gliding arc plasma reactor, *Chem. Eng. J.* 443 (2022) 136529.
- [8] P. Lamichhane, N. Pourali, E.V. Rebrov, V. Hessel, Energy Intensified Nitrogen Fixation Through Fast Modulated Gas Discharge from Pyramid-shaped Micro-electrode, *Plasma Chem. Plasma Process.* (2023) 1–24.
- [9] W. Wang, D. Mei, X. Tu, A. Bogaerts, Gliding arc plasma for CO₂ conversion: Better insights by a combined experimental and modelling approach, *Chem. Eng. J.* 330 (2017) 11–25.
- [10] O. Samadi Bahnamiri, F. Manaigo, A. Chatterjee, R. Snyders, F. A. D'Isa, and N. Britun, "Investigation of nitrogen fixation in low-pressure microwave plasma via rotational–vibrational NO and N₂ kinetics," *Journal of Applied Physics*, vol. 133, 2023.
- [11] S. Kelly, A. Bogaerts, Nitrogen fixation in an electrode-free microwave plasma, *Joule* 5 (2021) 3006–3030.
- [12] V. Hessel, G. Cravotto, P. Fitzpatrick, B. Patil, J. Lang, W. Bonrath, Industrial applications of plasma, microwave and ultrasound techniques: Nitrogen-fixation and hydrogenation reactions, *Chem. Eng. Process.* 71 (2013) 19–30.
- [13] S. Kelly, C. Verheyen, A. Cowley, A. Bogaerts, Producing oxygen and fertilizer with the Martian atmosphere by using microwave plasma, *Chem* 8 (2022) 2797–2816.
- [14] N. Saksono, P. Suryawinata, Z. Zakaria, B. Farawan, Fixation of air nitrogen to ammonia and nitrate using cathodic plasma and anodic plasma in the air plasma electrolysis method, *Environ. Prog. Sustain. Energy* 43 (2024) e14331.
- [15] C. Fromentin, T. Silva, T. Dias, E. Baratte, O. Guaitella, V. Guerra, Validation of non-equilibrium kinetics in CO₂–N₂ plasmas, *Plasma Sources Sci. Technol.* 32 (2023) 054004.
- [16] M. Majeed, M. Iqbal, M. Altin, Y.-N. Kim, D.K. Dinh, C. Lee, et al., Effect of thermal gas quenching on NO_x production by atmospheric pressure rotating arc plasma: a pathway towards eco-friendly fertilizer, *Chem. Eng. J.* 485 (2024) 149727.
- [17] B.N. Bayer, P.J. Bruggeman, A. Bhan, NO formation by N₂/O₂ plasma catalysis: The impact of surface reactions, gas-phase reactions, and mass transport, *Chem. Eng. J.* 482 (2024) 149041.
- [18] N. Kaushik, S. Mitra, E.J. Baek, L.N. Nguyen, P. Bhartiya, J.H. Kim, et al., The inactivation and destruction of viruses by reactive oxygen species generated through physical and cold atmospheric plasma techniques: Current status and perspectives, *J. Adv. Res.* 43 (2023) 59–71.
- [19] P. Shaw, N. Kumar, H.S. Kwak, J.H. Park, H.S. Uhm, A. Bogaerts, et al., Bacterial inactivation by plasma treated water enhanced by reactive nitrogen species, *Sci. Rep.* 8 (2018) 11268.
- [20] N.K. Kaushik, P. Bhartiya, N. Kaushik, Y. Shin, L.N. Nguyen, J.S. Park, et al., Nitric oxide enriched plasma-activated water inactivates 229E coronavirus and alters antiviral response genes in human lung host cells, *Bioact. Mater.* 19 (2023) 569–580.
- [21] M. Bagheri, M. Mohseni, Computational fluid dynamics (CFD) modeling of VUV/UV photoreactors for water treatment, *Chem. Eng. J.* 256 (2014) 51–60.
- [22] P. Wollny, J. Menser, L. Engelmann, J. Sellmann, C. Schulz, H. Wiggers, et al., The role of phase transition by nucleation, condensation, and evaporation for the synthesis of silicon nanoparticles in a microwave plasma reactor—Simulation and experiment, *Chem. Eng. J.* 453 (2023) 139695.
- [23] J. Van Dijk, G. Kroesen, A. Bogaerts, Plasma modelling and numerical simulation, *J. Phys. D Appl. Phys.* 42 (2009) 190301.
- [24] O. Sedej, E. Mbonimpa, CFD Modeling of a Lab-Scale Microwave Plasma Reactor for Waste-to-Energy Applications: A Review, *Gases* 1 (2021) 133–147.
- [25] S. Wang, V. Rohani, P. Dupont, S. Pagnon, L. Fulcheri, A chemical kinetics simulation of plasma-catalytic dry reforming, *Chem. Phys.* 574 (2023) 112017.
- [26] M.Y. Ong, S.R. Chia, J. Milano, S. Nomanbhay, K.W. Chew, T. Yusaf, et al., Simulation of argon-excited microwave plasma reactor for green energy and CO₂ conversion application, *Appl. Energy* 353 (2024) 122160.
- [27] M. Abdollahzadeh, J. Pascoa, P. Oliveira, Implementation of the classical plasma–fluid model for simulation of dielectric barrier discharge (DBD) actuators in OpenFOAM, *Comput. Fluids* 128 (2016) 77–90.
- [28] S. Pancheshnyi, B. Eismann, G. Hagelaar, L. Pitchford, ZDPlasKin: a new tool for plasmachemical simulations, *Bull. Am. Phys. Soc.* 53 (2008).
- [29] S. Van Alphen, A. Hecimovic, C.K. Kiefer, U. Fantz, R. Snyders, A. Bogaerts, Modelling post-plasma quenching nozzles for improving the performance of CO₂ microwave plasmas, *Chem. Eng. J.* 462 (2023) 142217.
- [30] J. Perambadur, A.Y. Klimenko, V. Rudolph, P. Shukla, Investigation of plasma swirl dynamics and effects of secondary gas injection in a vortex gas stabilized DC arc plasma, *Int. J. Heat Fluid Flow* 95 (2022) 108978.

- [31] T. Butterworth, A. Van de Steeg, D. Van den Bekerom, T. Minea, T. Righart, Q. Ong, et al., Plasma induced vibrational excitation of CH₄—a window to its mode selective processing, *Plasma Sources Sci. Technol.* 29 (2020) 095007.
- [32] A. Van de Steeg, T. Butterworth, D. Van den Bekerom, A. Silva, M. Van de Sanden, G. Van Rooij, Plasma activation of N₂, CH₄, and CO₂: an assessment of the vibrational non-equilibrium time window, *Plasma Sources Sci. Technol.* 29 (2020) 115001.
- [33] D.A. Long, *The Raman effect, A Unified Treatment of the Theory of Raman Scattering by Molecules*, The Raman Effect, 2002.
- [34] M.A. Buldakov, V.N. Cherepanov, B.V. Korolev, I.I. Matrosov, Role of intramolecular interactions in Raman spectra of N₂ and O₂ molecules, *J. Mol. Spectrosc.* 217 (2003) 1–8.
- [35] K.-P. Huber, Constants of diatomic molecules, *Molecular Spectra and Molecular Structure* 4 (1979) 146–291.
- [36] A. Lofthus, P.H. Krupenie, The spectrum of molecular nitrogen, *J. Phys. Chem. Ref. Data* 6 (1977) 113–307.
- [37] J. Bendtsen, The rotational and rotation-vibrational Raman spectra of 14N₂, 14N15N and 15N₂, *J. Raman Spectrosc.* 2 (1974) 133–145.
- [38] G. Herzberg, *Molecular Spectra and Molecule Structure. I. Diatomic Molecules*, *J. Phys. Chem.* 44 (1940) 954.
- [39] C. Park, Review of chemical-kinetic problems of future NASA missions. I-Earth entries, *J. Thermophys Heat Transfer* 7 (1993) 385–398.
- [40] J.D. Anderson, *Hypersonic and high-temperature gas dynamics*, Aiaa (1989).
- [41] R. N. Gupta, “A Review of reaction rates and thermodynamic and transport properties for the 11-species air model for chemical and thermal nonequilibrium calculations to 30000K,” J. M. Yos and R. A. Thompson, Eds., ed. Hampton, Va.: National Aeronautics and Space Administration, Langley Research Center, 1989.
- [42] R.B. Bird, W.E. Stewart, E.N. Lightfoot, R.E. Meredith, *Transport phenomena*, *J. Electrochem. Soc.* 108 (1961) 78C.
- [43] B. Andersson, R. Andersson, L. Håkansson, M. Mortensen, R. Sudiyo, B. Van Wachem, *Computational fluid dynamics for engineers*, Cambridge University Press, 2011.